Ultrasonics Sonochemistry 101 (2023) 106715

Contents lists available at ScienceDirect

Ultrasonics Sonochemistry

journal homepage: www.elsevier.com/locate/ultson

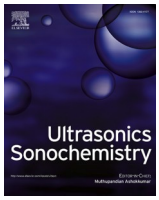

Revealing the origins of vortex cavitation in a Venturi tube by high speed X-ray imaging

Hitoshi Soyama [a,*], Xiaoyu Liang [b], Wataru Yashiro [c,b,d], Kentaro Kajiwara [e], Eleni Myrto Asimakopoulou [f], Valerio Bellucci [g], Sarlota Birnsteinova [g], Gabriele Giovanetti [g], Chan Kim [g], Henry J. Kirkwood [g], Jayanath C.P. Koliyadu [g], Romain Letrun [g], Yuhe Zhang [f], Jozef Uličný [h], Richard Bean [g], Adrian P. Mancuso [i,j], Pablo Villanueva-Perez [f], Tokushi Sato [g], Patrik Vagovič [k,g], Daniel Eakins [l], Alexander M. Korsunsky [l]

[a] Department of Finemechanics, Tohoku University, 6-6-01 Aramaki, Aoba-ku, Sendai 980-8579, Japan
[b] Institute of Multidisciplinary Research for Advanced Materials (IMRAM), Tohoku University, Katahira 2-1-1, Aoba-ku, Sendai, Miyagi 980-8577, Japan
[c] International Center for Synchrotron Radiation Innovation Smart (SRIS), Tohoku University, Katahira 2-1-1, Aoba-ku, Sendai, Miyagi 980-8577, Japan
[d] Department of Applied Physics, School of Engineering, The University of Tokyo, 7-3-1 Hongo, Bunkyo-ku, Tokyo 113-8656, Japan
[e] Japan Synchrotron Radiation Research Institute, 1-1-1 Kouto, Sayo, Hyogo 679-5198, Japan
[f] Synchrotron Radiation Research and NanoLund, Lund University, Box 118, Lund, 221 00, Sweden
[g] European XFEL GmbH, Holzkoppel 4, 22869 Schenefeld, Germany
[h] Faculty of Science, Department of Biophysics, P. J. Šafárik University, Jesenná 5, 04154 Košice, Slovakia
[i] Diamond Light Source Ltd, Harwell Science and Innovation Campus, Diamond House, Didcot, OX11 0DE, UK
[j] Department of Chemistry and Physics, La Trobe Institute for Molecular Science, La Trobe University, Melbourne, Victoria 3086, Australia
[k] Center for Free-Electron Laser (CFEL), DESY, Notkestraße 85, 22607 Hamburg, Germany
[l] Department of Engineering Science, University of Oxford, Parks Road, Oxford OX1 3PJ, UK

ARTICLE INFO

Keywords:
Hydrodynamic cavitation
Vortex
Bubble
X-ray imaging

ABSTRACT

Hydrodynamic cavitation is useful in many processing applications, for example, in chemical reactors, water treatment and biochemical engineering. An important type of hydrodynamic cavitation that occurs in a Venturi tube is vortex cavitation known to cause luminescence whose intensity is closely related to the size and number of cavitation events. However, the mechanistic origins of bubbles constituting vortex cavitation remains unclear, although it has been concluded that the pressure fields generated by the cavitation collapse strongly depends on the bubble geometry. The common view is that vortex cavitation consists of numerous small spherical bubbles. In the present paper, aspects of vortex cavitation arising in a Venturi tube were visualized using high-speed X-ray imaging at SPring-8 and European XFEL. It was discovered that vortex cavitation in a Venturi tube consisted of angulated rather than spherical bubbles. The tangential velocity of the surface of vortex cavitation was assessed considering the Rankine vortex model.

1. Introduction

Hydrodynamic cavitation has attracted attention in various contexts including chemical reactors [1,2], water treatment [3–5], biochemical engineering [6], synthesis of biodiesel [7–9], *ex-situ* biological hydrogen methanation [10], as well as degradation of harmful substances such as bisphenol [11], sulfamerazine [12], ammonia nitrogen [13], fatty acid [14], microcystis aeruginosa [15]. Several types of cavitating devices have been proposed, such as Venturi type [16], jet type [17], swirling vortex type [18] and rotor type [19]. In most cases, cavitation was not observed directly, so it was assumed to consist of spherical bubble(s) [20,21], even in the case of acoustic cavitation [22].

Experimental and numerical analyses were performed for cavitation reactors that use hydrodynamic cavitation. The cavitation performance of a rotor-radial groove (RRG) hydrodynamic cavitation reactor was analyzed using computational fluid dynamics to investigate the cavitating region without observing the cavitation [19]. The liquid–liquid emulsions were investigated experimentally using a vortex-based

* Corresponding author.
E-mail address: soyama@mm.mech.tohoku.ac.jp (H. Soyama).

https://doi.org/10.1016/j.ultsonch.2023.106715
Received 19 September 2023; Received in revised form 18 November 2023; Accepted 1 December 2023
Available online 3 December 2023

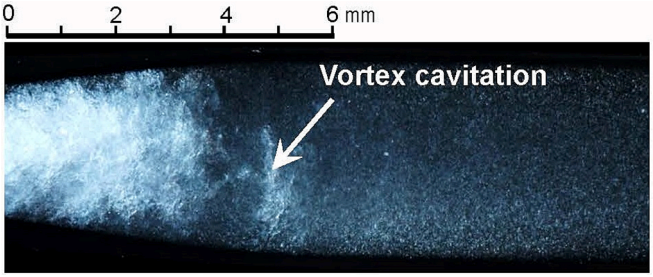

Fig. 1. Typical vortex cavitation arising in Venturi tube [16].

hydrodynamic cavitation unit [23]; however, cavitation was not observed. The cavitation noise of hydrodynamic cavitation arising in jet pump cavitation reactors (JPCRs) was measured whilst varying the throat lengths, throat types, and diffuser angles and observing vortex cavitation, and the averaged aspects were discussed [17]. The mixing performance of a consecutive competing reaction system was numerically investigated in a swirling vortex flow reactor (SVFR) considering turbulent eddies [18]. The cavitation cloud shedding and cavitating regions were simulated using bubble dynamics and compared with experimental results [24]. Although cloud cavitation and horseshoe cavitation were observed in a Venturi tube, the discussions of these phenomena were based on the assumption of spherical bubbles [25]. The re-entrant flow arising in a Venturi tube was also simulated [21]; however, the cavitating region was also assumed to consist of small spherical bubbles. Cloud cavitation arising in a Venturi tube [26] was recognized and simulated numerically; it was assumed that cloud cavitation consisted of small spherical bubbles [27]. It is concluded that hydrodynamic cavitation in various systems has so far been only evaluated experimentally as systems of spherical bubble. Numerical simulation of ultrasonic cavitation was also performed. Once again, bubble dynamics was simulated using spherical bubbles [22]. Non-spherical bubbles were observed in ultrasonic cavitation, but it has so far proved impossible to extract further details [28]. In [20], the cases of both hydrodynamic and ultrasonic cavitation were considered spherical bubble(s). Intense cavitation is an infrequent event in both hydrodynamic [29] and ultrasonic cavitation [30]. For example, it was noted in [29] that only a few of 1000 cavitation clouds (less than 1 %) produced strong impacts, and only a few large impacts were generated by vibrations at 20 kHz [30]. If the mechanisms of cavitation could be elucidated, the efficiency of cavitation reactors and/or cavitation peening would be drastically improved.

With respect to the numerical simulation of cloud cavitation, a model of cloud cavitation consisting of small spherical bubbles has been proposed [31], and numerical simulations were carried out considering cavitation-vortex interaction [32], the interaction of bubbles [33], the effect of cavitation on local flow pattern [34], surface tension [35], position of bubbles [36], and collapse of clouds [37]. In conventional numerical simulations of cloud cavitation, it is assumed that cloud cavitation consists of small spherical bubbles. However, recent numerical and experimental investigations of bubble dynamics have suggested that the intensity of a single bubble collapse is strongly affected by the geometry of the bubble and the distance between the bubble and the rigid wall [38,39]. Higher fidelity simulation of cavitation can be achieved using conventional computational fluid dynamics if bubbles could be assumed to be non-spherical. As the effect of non-condensable gas was also revealed by a new Euler-Lagrangian cavitation model [40], the investigation of structure of vortex cavitation will helpful to develop the simulations.

As reviewed by Arndt [41], cloud cavitation has the form of a vortical flow. Typical vortex cavitation is the “tip vortex cavitation” which occurs at the tip of a screw propeller [42]. In the present work, the term “vortex cavitation” is used to describe the cavitation, as shown in Fig. 1 [16]. Note that the luminescence intensity induced by the

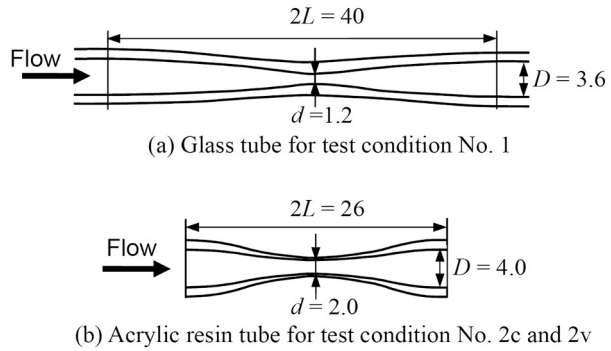

Fig. 2. Schematic geometry of the Venturi tube. (a) Glass tube for test condition No. 1. (b) Acrylic resin tube for test condition No. 2c and 2v

hydrodynamic cavitation in a Venturi tube is proportional to the shedding frequency and size of the vortex cavitation [16]. Vortex cavitation is a key factor in the aggressive intensity of hydrodynamic cavitation. The conventional model of vortex cavitation is based on the observation of vortex cavitation on a hydrofoil [43] and consists of small spherical bubbles. It is still used for unsteady cavitating flows [44] and cavitating flows around hydrofoils [45,46]. In another model of vortex cavitation, the surface of the vortex is smooth [47].

In the investigation of the cavitation cloud by X-rays, the void fraction of cloud cavitation around the Venturi [48–50] and hydrofoil [51–56] were evaluated. Vapor bubbles in the Venturi tube profile were detected at 3,000 frames per second using synchrotron radiation at the XOR 32-ID beamline of the Advanced Photon Source (APS), Argonne National Laboratory (ANL) [57]. The time averaged aspect of ultrasonic cavitation was also visualized by synchrotron radiation at the BMIT-BM 05B1-1 beamline of the Canadian Light Source (CLS) [58]. The dynamic behavior of ultrasonic cavitation also investigated at I13-2 Diamond-Manchester Imaging Branchline of Diamond Light Source, UK [59–61], and the quasi-static bubble oscillation was reported [60,61]. Radiographs of the cavitating flow through the nozzle were captured at 12,070 frames per second [62–64], then 67,890 frames per second [65,66] at the APS in ANL. The non-spherical bubble in the attached cavitation was recognized [62–64,66]. High-speed, kHz sampling rate 4D tomography has be achieved using synchrotron radiation [67,68], whilst imaging rates exceeding a MHz are now possible using an X-ray free electron laser (XFEL) [69].

When the aggressive intensity of hydraulic cavitation through Venturi tube was evaluated by cavitation noise [70], a few pulses of intense cavitation noise were detected per second, although hundreds of clouds and/or vortex cavitation were generated as same as an impinging cavitating jet [71]. In the present study, in order to improve drastically the efficiency of a cavitation reactor using hydrodynamic cavitation, the behavior of vortex cavitation arising in a Venturi tube was observed by high-speed radiography using X-ray illumination at SPring-8 and European-XFEL. It was found that vortex cavitation consisted of angulated bubbles rather than spherical bubbles. The tangential velocity of the surface of vortex cavitation was also evaluated by considering the Rankine vortex, similar to the case of cavitation around the heart valve [72] and tip vortex cavitation [73].

2. Experimental apparatus and procedures

Fig. 2 shows the schematic of Venturi tubes made of glass and acrylic resin in this work. In Fig. 2, d and D are the throat diameter and the inner diameter of the Venturi tube, respectively, and L is the length of the contraction-and-expansion-part of the Venturi tube. For $d = 1.2$ mm in Table 1, L was 20 mm, as in a previous report [16]. For all other Venturi tube, L was chosen based on the field of view at the observation. Table 1 lists the materials of the Venturi tube and the hydrodynamic test

Table 1
Schematics of the Venturi tube and hydrodynamic test condition.

Symbol	Material	Diameter of throat d mm	Diameter of tube D mm	Upstream pressure p_1 MPa	Downstream pressure p_2 MPa	Temperature t_w °C	Velocity at throat U m/s	Reynolds number	Cavitation number
No. 1	Glass	1.2	3.6	0.560 ± 0.028	0.166 ± 0.008	26 ± 2	28.1 ± 1.0	(3.9 ± 0.1) × 10^4	0.41 ± 0.03
No. 2c	Acrylic resin	2.0	4.0	0.377 ± 0.019	0.180 ± 0.009	26 ± 2	19.8 ± 1.1	(4.5 ± 0.2) × 10^4	0.90 ± 0.10
No. 2v	Acrylic resin	2.0	4.0	0.078 ± 0.004	0.027 ± 0.001	26 ± 2	10.1 ± 0.4	(2.3 ± 0.1) × 10^4	0.47 ± 0.04
No. 3	Acrylic resin	0.5	3.0	0.350 ± 0.035	0.100 ± 0.001	21 ± 2	22.4 ± 1.5	(1.1 ± 0.1) × 10^4	0.39 ± 0.05

Note. – Pressures given are absolute pressure.

Table 2
Test conditions for visualization of the vortex cavitation by X-rays.

	Used test loop of Venturi tube (see Fig. 3)	Test site, Beam line	Field of view (mm × mm) [pixel × pixel]	Recording speed (frame/sec)
No. 1	Compression type	SPring-8, BL28B2	(13.5 mm × 6.75 mm) [1280 pixel × 640 pixel]	69,600
No. 2c	Compression type			
No. 2v	Vacuum type			
No. 3	Diaphragm pump type	European-XFEL, SPB/SFX	(1.28 mm × 0.8 mm) [400 pixel × 250 pixel]	1,128,668

conditions. The "c" and "v" letters associated with No. 2 denote the compression type and vacuum type test loop, respectively. To investigate the vortex cavitation arising in the Venturi tube, three types of Venturi tubes were prepared considering the material transparency to X-ray and fluid dynamics parameters, such as the Reynolds number and velocity at the throat, as listed in Table 1. Table 2 lists the test conditions for the X-ray visualization of the vortex cavitation phenomenon.

Reynolds number, Re, was defined by d, the flow velocity at the throat U and kinematic viscosity of water ν_w, and U was obtained from the pressure difference between the upstream pressure p_1 and downstream pressure p_2 of the throat, as follows:

$$Re = \frac{dU}{\nu_w} = \frac{d\sqrt{\frac{2}{\rho}(p_1 - p_2)}}{\nu_w}, \tag{1}$$

where ρ is the density of water.

The cavitation number σ was defined by p_1, p_2 and the vapor pressure of water p_v as,

$$\sigma = \frac{p_1 - p_2}{\frac{1}{2}\rho U^2} = \frac{p_2 - p_v}{p_1 - p_2}. \tag{2}$$

Fig. 3 illustrates the three types of test loops of hydrodynamic cavitation through a Venturi tube. In configuration (a) compression type, compressed air was charged in the pressure tank using a compressor, and the test water was installed in tank 1. After the beamline hutch door was interlocked, valve 1, which was an electromagnetic valve, was opened, and the test water was passed through a Venturi tube to generate hydrodynamic cavitation.

A vacuum type setup was conceived to reduce the cavitation number and flow velocity in the Venturi tube. In (b) vacuum type, the air in Tank 2 was evacuated using a vacuum pump. Valve 1 was opened after the hutch door was interlocked, and the water stored in tank 1 flowed through the Venturi tube to tank 2 as $p_1 > p_2$.

Fig. 3(c) illustrates a diaphragm pump type similar to that used in a previous report [16]. Test water, pressurized using a diaphragm pump, was injected through the Venturi tube and returned to the tank. For all three types, the upstream and downstream pressures were measured using pressure gauges, and the pressures were controlled by the downstream valve, and either the pressure/vacuum in the tanks or the rotational speed of the diaphragm pump.

Test condition No. 1 was chosen as that of the previous study on vortex cavitation arising in a Venturi tube [16]. As the main purpose of the present study was to use X-ray to visualize and investigate the bubbles in vortex cavitation, the choice of Reynolds number was an important factor. Test condition No. 2c was chosen to match the Reynolds number used in test No. 1, i.e., $Re \approx 4 \times 10^4$, considering the field of view and recording speed, by increasing the throat diameter d to decrease U (see Eq. (1)). To investigate vortex cavitation more clearly, test condition No. 2v was chosen to reduce the flow velocity U at a similar cavitation number to test No. 1, i.e. $\sigma \approx 0.4$, by decreasing the pressures p_1 and p_2 (see Eq. (2)). In the European XFEL test No. 3, Megahertz capture rates are available [69,74]; however, the field of view is limited. Consequently, $d = 0.5$ mm was chosen and the cavitation number was set similar to that of test No. 1, i.e., $\sigma \approx 0.4$.

The uncertainties of measured upstream pressure and downstream pressure were shown in Table 1. Note that the pressures of compressive type and vacuum type were slightly decreased due to the volume of pressure tank and vacuum tank. In the case of diaphragm pump type, the upstream pressure was fluctuated about 10 % due to the diaphragm pump [16]. As U was obtained from p_1 and p_2, the uncertainty of U, Re and σ were obtained as shown in Table 1 considering error analysis [75].

The experiments were conducted on two beamlines, BL28B2 at SPring-8, Japan [67] and SPB-SFX at European-XFEL, DESY, Germany [76]. High-speed cameras were used to visualize vortex cavitation. The field-of-view and recording speed for each test are listed in Table 2. The spatial resolution of X-ray imaging was 10.5 μm/pixel for BL28B2 and 2.5 μm/pixel for SPB-SFX. At BL28B2, SPring-8, the aspect of vortex cavitation was simultaneously observed by visible light using a high-speed video camera at 21,600 frames per second. A high-speed video camera for X-rays was aligned horizontally, while the visible light camera was placed at the inclination of 18.9° below horizontal, as shown in Fig. 4. The details of high-speed photography using X-rays are provided in references [67–69,74,76].

3. Results

3.1. Periodical shedding of vortex cavitation

Figs. 5 and 6 show the aspects of hydrodynamic cavitation through a Venturi tube using visible light and X-rays. The direction of the main flow through the Venturi tube in Figs. 5 and 6 was from the left side to the right side. In the present study, to show images in the same flow direction for both images observed by visible light and X-rays, the left and right sides of the images observed by visible light were reversed. The four-digit numbers in each frame in Figs. 5 and 6 reveal the time in milliseconds. The test condition of Figs. 5 and 6 was "No. 1" in Tables 1 and 2. In the present study, we focused on vortex cavitation and observed the area around the trailing edge of the cavitating region, as it was found that the collapse of the vortex cavitation produced intensive

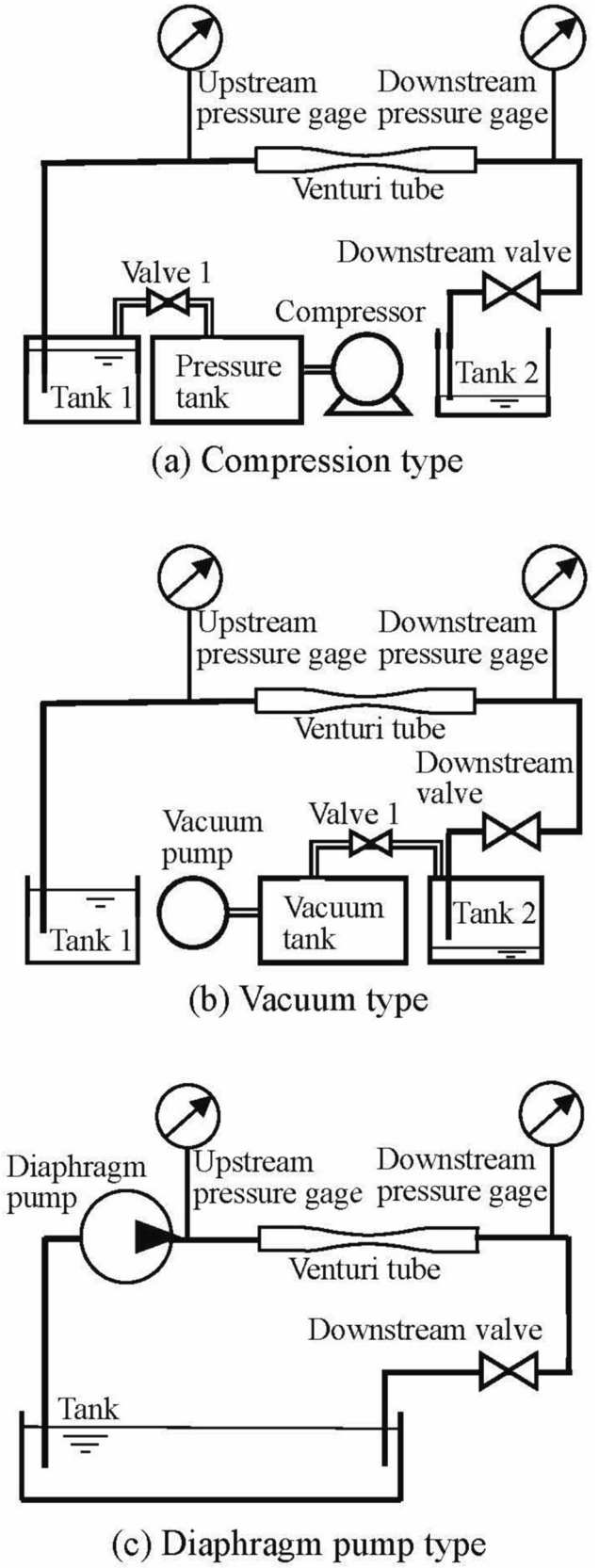

Fig. 3. Schematics of the test loop of hydrodynamic cavitation through Venturi tube.

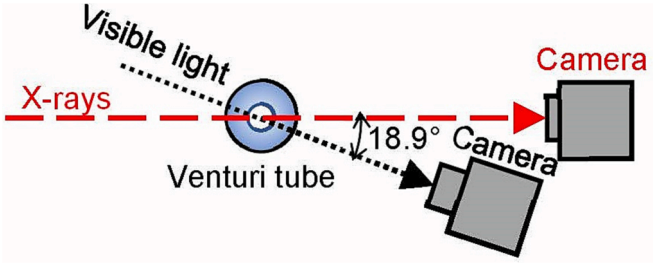

Fig. 4. Positions of cameras at BL28B2, SPring-8.

collapse [16]. This vortex cavitation was similar to horseshoe vortex cavitation which was shedding from the attached and/or cloud cavitation on hydrofoil [43,64,77,78], and it was revealed that the horseshoe vortex cavitation was severely erosive cavitation [77,78]. Based on earlier report [16], the trailing edge is indicated by dotted yellow lines in Fig. 5 to identify the periodical shedding of the vortex cavitation. When the time interval of the shedding of vortex cavitation in Fig. 5 was considered, we found that for the cases shown it was 0.093–0.417 ms, 0.417–0.972 ms, 0.972–1.296 ms, 1.296–1.574 ms, 1.574–1.713 ms, 1.713–2.407 ms, 2.407–2.546 ms, 2.546–2.870 ms, i.e., the duration of sequential vortex cavitation shedding were 0.342 ms, 0.556 ms, 0.324 ms, 0.278 ms, 0.139 ms, 0.694 ms, 0. 139 ms, and 0.324 ms, respectively. These seem like almost multiples of 0.14 ms with the exception of 0.324 ms and 0.342 ms. The subharmonic frequency, which was the lowest shedding frequency, was ~ 1.44 kHz. It is similar to the value reported in a previous study [16], i.e., c_0 (688 σ + 961) = 1.24 ± 0.12 kHz. Here, c_0 is constant and equal to 1 Hz. In the previous experiment [16], test water was pressurized by the diaphragm pump, which produced pressure fluctuation at 57.0 ± 2.5 Hz. In the present experiment, the test water was injected into the Venturi tube more stably using pressurized air, as shown in Fig. 3 (a). In other words, vortex cavitation was periodically shed by injecting stable conditions.

By observing the trailing edge of the cavitating region, that is, the slope of the dotted yellow lines in Fig. 5, considering the frame interval, the shedding velocity of vortex cavitation near the trailing edge was 7.9 ± 2.6 m/s. In Fig. 5, the remarkable vortex cavitation sequences are indicated by yellow arrows. The distance between vortex cavitation was 1.66 ± 0.08 mm; subsequently, the time interval of vortex cavitation shedding was 0.21 ± 0.07 ms and it corresponded to 4.8 ± 1.6 kHz. Thus, it can be concluded that the small vortex cavitations combined together, forming a large vortex cavitation, as 4.8 kHz > 1.44 kHz.

The remarkable features of vortex cavitation observed under visible light and X-rays illumination are shown in Figs. 5 and 6 and indicated by the arrow(s). Note that the observation angles of visible light (Fig. 5) and X-rays (Fig. 6) were slightly different, as shown in Fig. 4. The time of capture was also different because the recording speeds were different, as shown in Table 2. As shown in Fig. 6, the typical vortex cavitation was indicated by the arrow at 0.330 ms. The topology of the vortex cavitation phenomena will be addressed in a later section.

3.2. Attached cavitation and vortex cavitation

To precisely investigate the relationship between vortex cavitation and attached cavitation that developed near the throat, the aspect of hydrodynamic cavitation through the Venturi tube, which was made of acrylic resin and whose L in Fig. 2 was approximately 13 mm, was observed using visible light and X-rays, as shown in Figs. 7 and 8. Fig. 8 (b) shows a magnified view of Fig. 8(a) from 1.538 ms to 1.596 ms. The test condition of Figs. 7 and 8 are shown as "No. 2c" in Tables 1 and 2, respectively. The main flow directions shown in Figs. 7 and 8 are from the left to right. Hydrodynamic cavitation was recorded at 21,600 fps using visible light; four skipped images are shown in Fig. 7. As shown in Fig. 7, the attached cavitation developed near the throat and the vortex

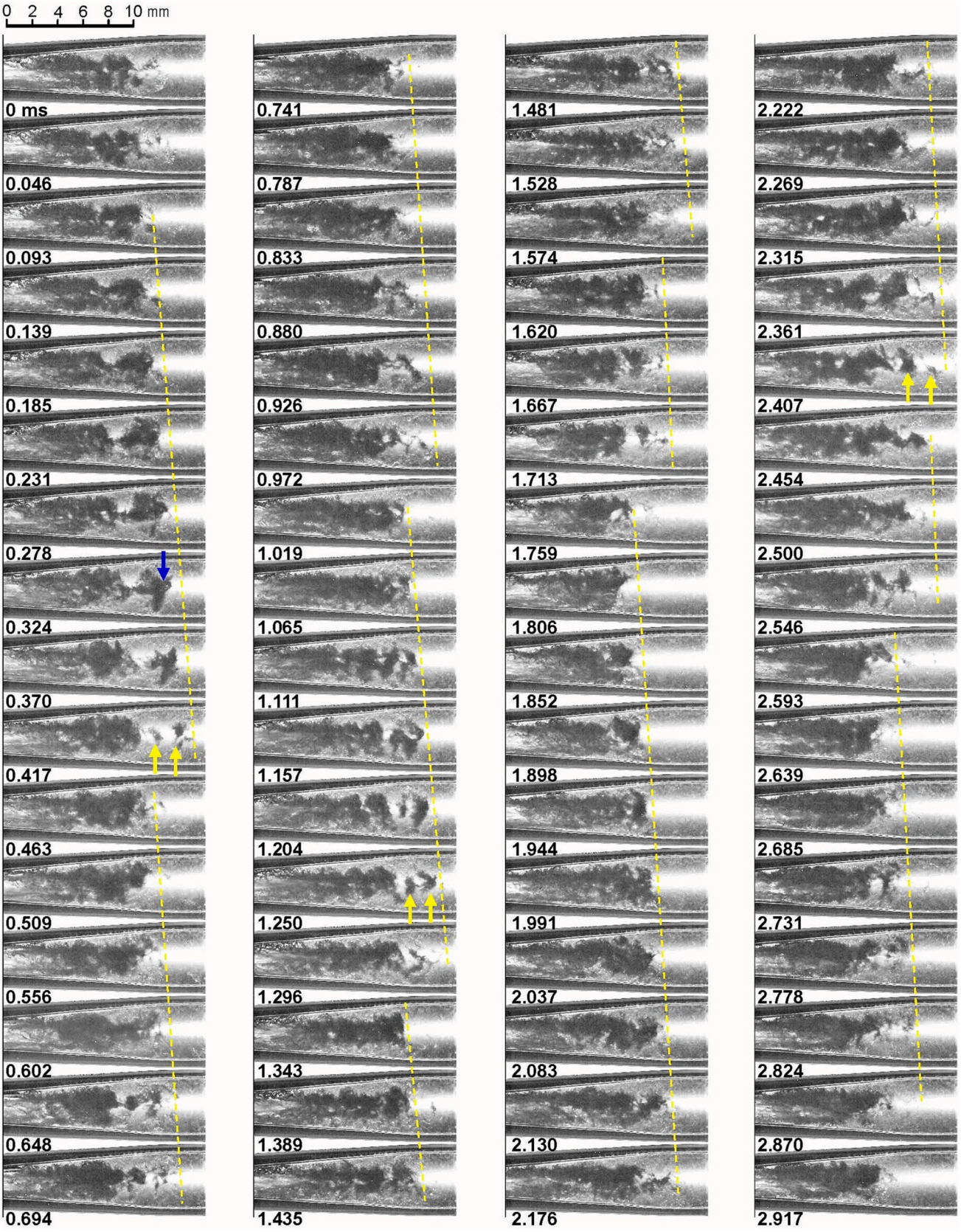

Fig. 5. Periodical shedding of vortex cavitation at $d = 1.2$ mm, $p_1 = 0.560$ MPa, $p_2 = 0.166$ MPa, $\sigma = 0.41$ observed by visible light.

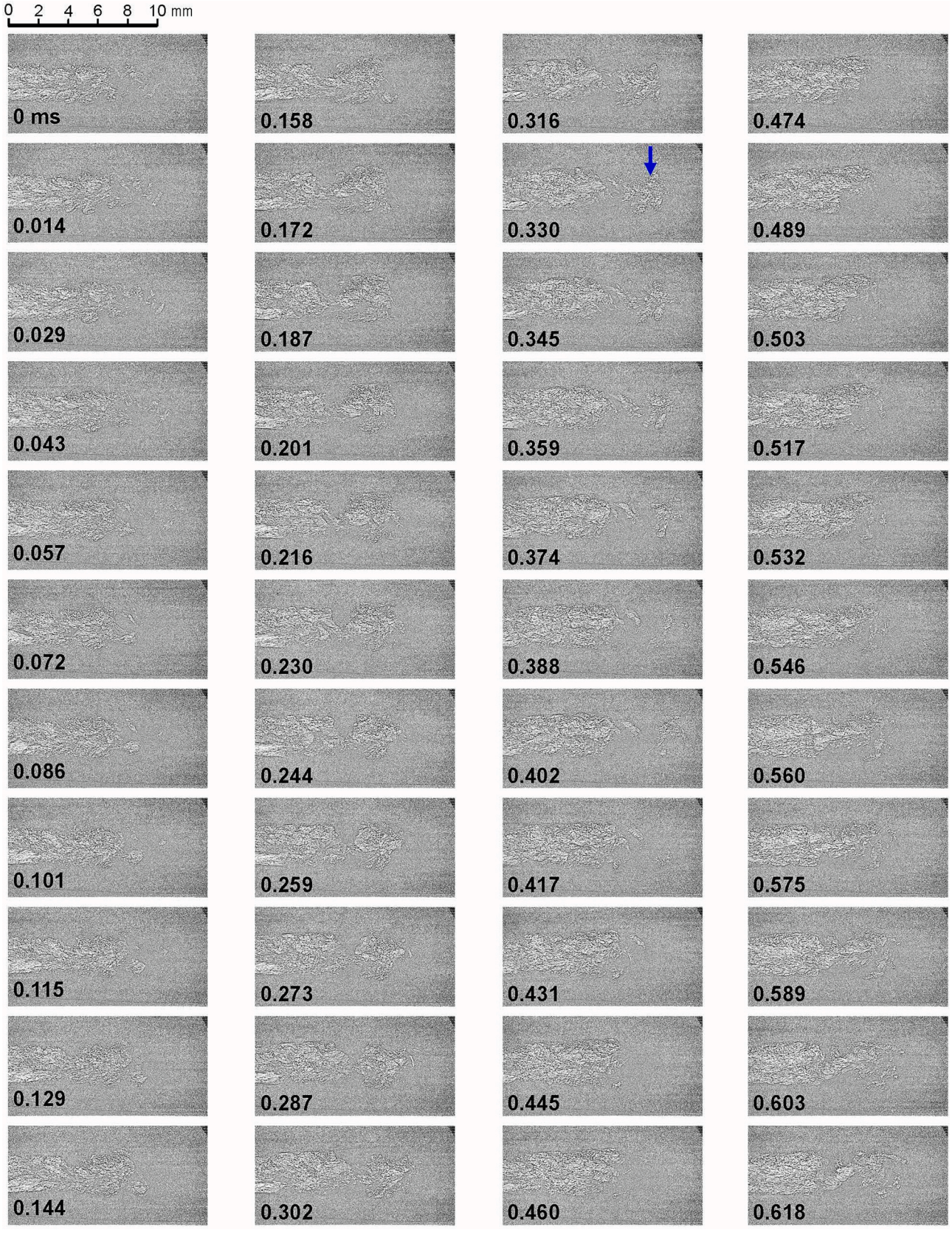

Fig. 6. One cycle of vortex cavitation from shedding of trailing edge to collapse at $d = 1.2$ mm, $p_1 = 0.560$ MPa, $p_2 = 0.166$ MPa, $\sigma = 0.41$ observed by high speed X-ray imaging.

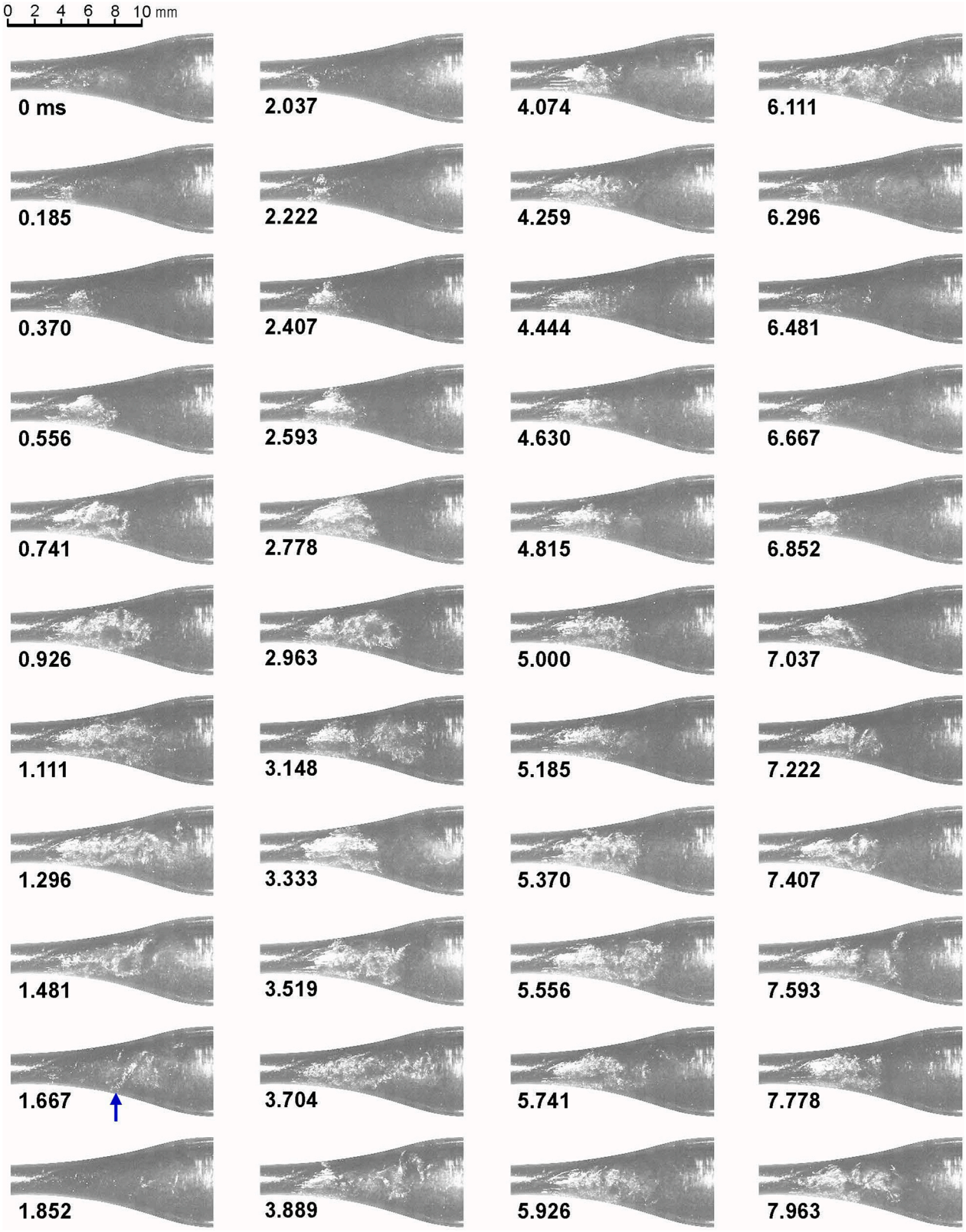

Fig. 7. Cyclic phenomena of cloud attached cavitation and vortex cavitation shedding at $d = 2.0$ mm, $p_1 = 0.377$ MPa, $p_2 = 0.180$ MPa, σ= 0.90 observed by visible light.

cavitation was mainly shed from the trailing edge of the attached cavitation. The minimum cavitating length was at 0.000 ms, 1.852 ms, 4.444 ms and 6.481 ms, and the time intervals of the vortex shedding were 1.852 ms, 2.593 ms and 2.037 ms, respectively. Thus, the shedding frequency of the vortex cavitation was about 470 ± 80 Hz. Compared to the shedding frequency of 1.6 kHz predicted from the current cavitation number, $\sigma = 0.90$, and the earlier relation for f_s [16], this represents a significant difference. This suggests that the shedding frequency of the

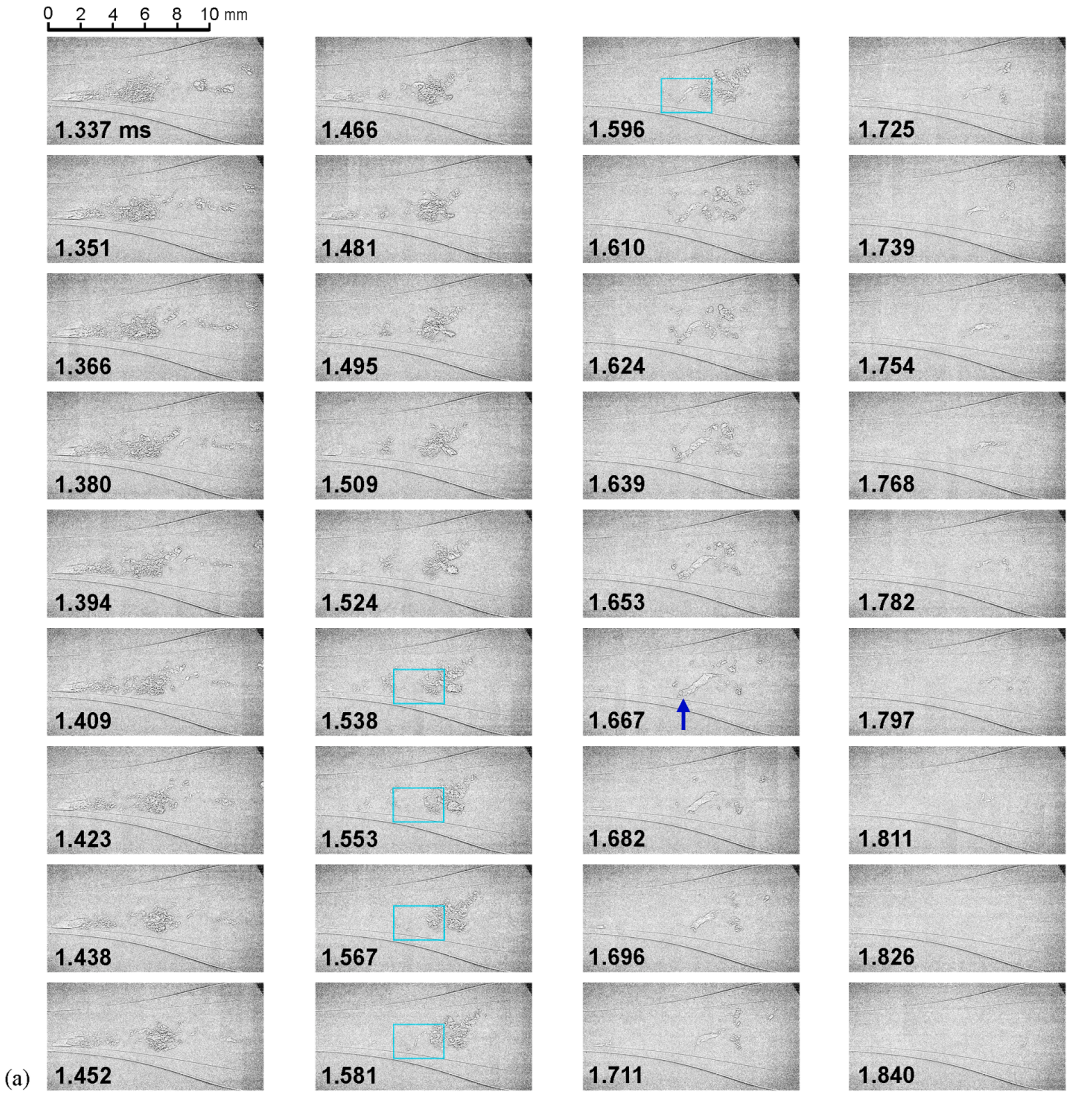

Fig. 8. Vortex cavitation from shedding of trailing edge to collapse at $d = 2.0$ mm, $p_1 = 0.377$ MPa, $p_2 = 0.180$ MPa, $\sigma = 0.90$, observed by high speed X-ray imaging. (a) Standard view of one cycle. (b) Magnified view

vortex cavitation through the Venturi tube depends also on the geometry of the Venturi tube.

To reveal the internal structure of vortex cavitation, the remarkable vortex cavitation in Figs. 7 and 8 is indicated by a blue arrow. The vortex cavitation at 1.667 ms in Fig. 7 and 1.667 ms in Fig. 8 is a longitudinal vortex cavitation with a vortex core inclined at 45° to the flow direction. The diameter of the vaporized core of the vortex cavitation at 1.667 ms was approximately 0.4 mm. The vaporized vortex core was composed of angulated rather than spherical bubbles. Now, we examine the initiation of this vortex cavitation using the magnified images shown in Fig. 8(b). The area of magnified view was indicated by light blue box in Fig. 8(a). At 1.538 ms and 1.553 ms, no bubbles were recognized in the region where the vortex cavitation was later observed. The region was indicated by a red rounded rectangle. The first bubbles were observed 14 μs later at 1.567 ms, which coalesced into a longitudinal vortex cavitation, which was indicated by a red arrow, a further 14 μs later at 1.581 ms. The diameter of the vaporized core of the vortex cavitation was about 0.1 mm at this time, which increases to ~ 0.15 mm at 1.596 ms. This result suggests that the vortex cavitation in the vortex core was generated by vortical flow. In the case of the visualization of a cavitating flow by X-rays, the depth of focus is considerably large compared to the observations using visible light, and the spatial resolution used was approximately 10 μm per pixel. These are significant advantages of the present observation method using X-rays. Thus, it can be concluded that there were no bubbles in this region. In the case of visualization using visible light, it is very hard to say “no bubble” due to its depth of focus and spatial resolution. Thus, it can be concluded by X-ray imaging that the vortex cavitation, which was observed at 1.667 ms in Figs. 7 and 8 (a), was initiated by a vortical flow without air bubbles downstream of the attached cavitation.

Figs. 7 and 8 show the two typical types of vortex cavitation. One type was generated by shedding part of the attached cavitation. In the second type, vortex cavitation was initiated by the vortical flow downstream of the attached cavitation. The vortical flow of the vortex cavitation is discussed in Section 3.4. *Tangential velocity of vortex cavitation*”.

3.3. *Angulated bubbles in vortex cavitation*

To precisely investigate the bubbles in vortex cavitation, Figs. 9 and 10 reveal the typical aspects of vortex cavitation arising in the Venturi tube observed by visible light and X-rays, as the shape and void ratio are closely related to the bubble collapse impact [38,39]. As mentioned previously, the conventional view is that vortex cavitation consists of small spherical bubbles. To examine the aspect of vortex cavitation, test

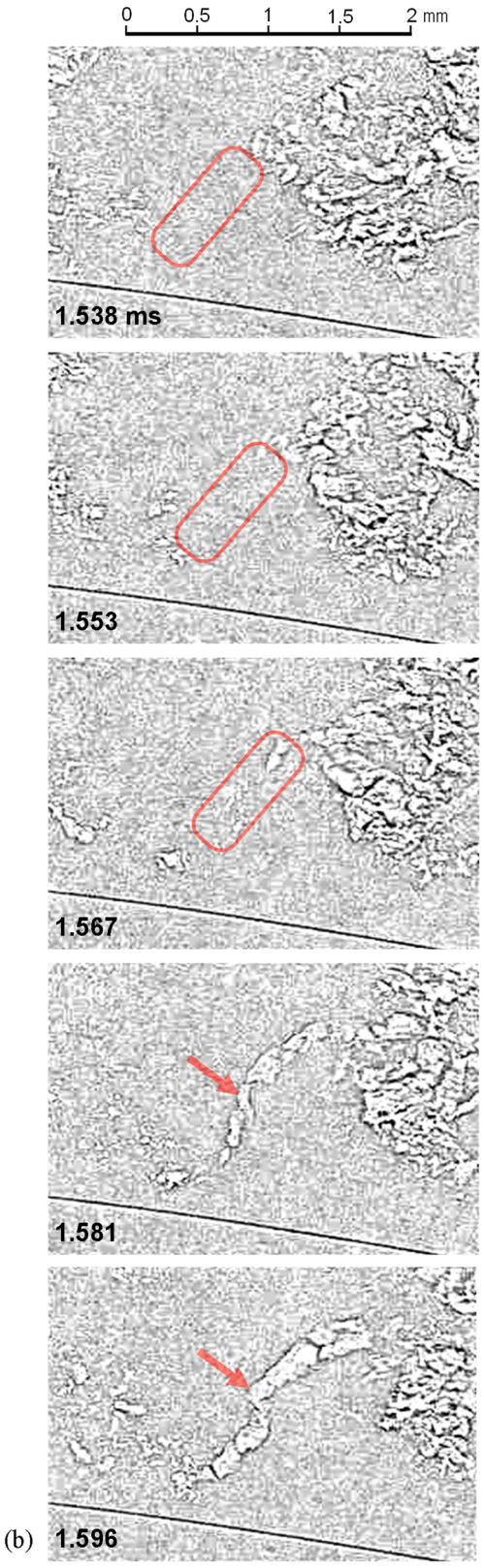

Fig. 8. (*continued*).

condition "No. 2v" was performed to decrease the flow velocity whilst maintaining a similar cavitation condition as "No. 1" with $\sigma \approx 0.4$. The main flow through the Venturi tube in Figs. 9 and 10 is from left to right. Notable vortex cavitation is indicated by a blue arrow at 0.926 ms in Figs. 9 and 10.

Notable vortex cavitation was initiated from the trailing edge of the attached cavitation and became longitudinal vortex cavitation, as shown in Fig. 9. When notable vortex cavitation was observed by the synchrotron, the vaporized vortex core consisted of angulated bubbles, as shown at 0.926 ms in Fig. 10. The bubbles in the vaporized core were

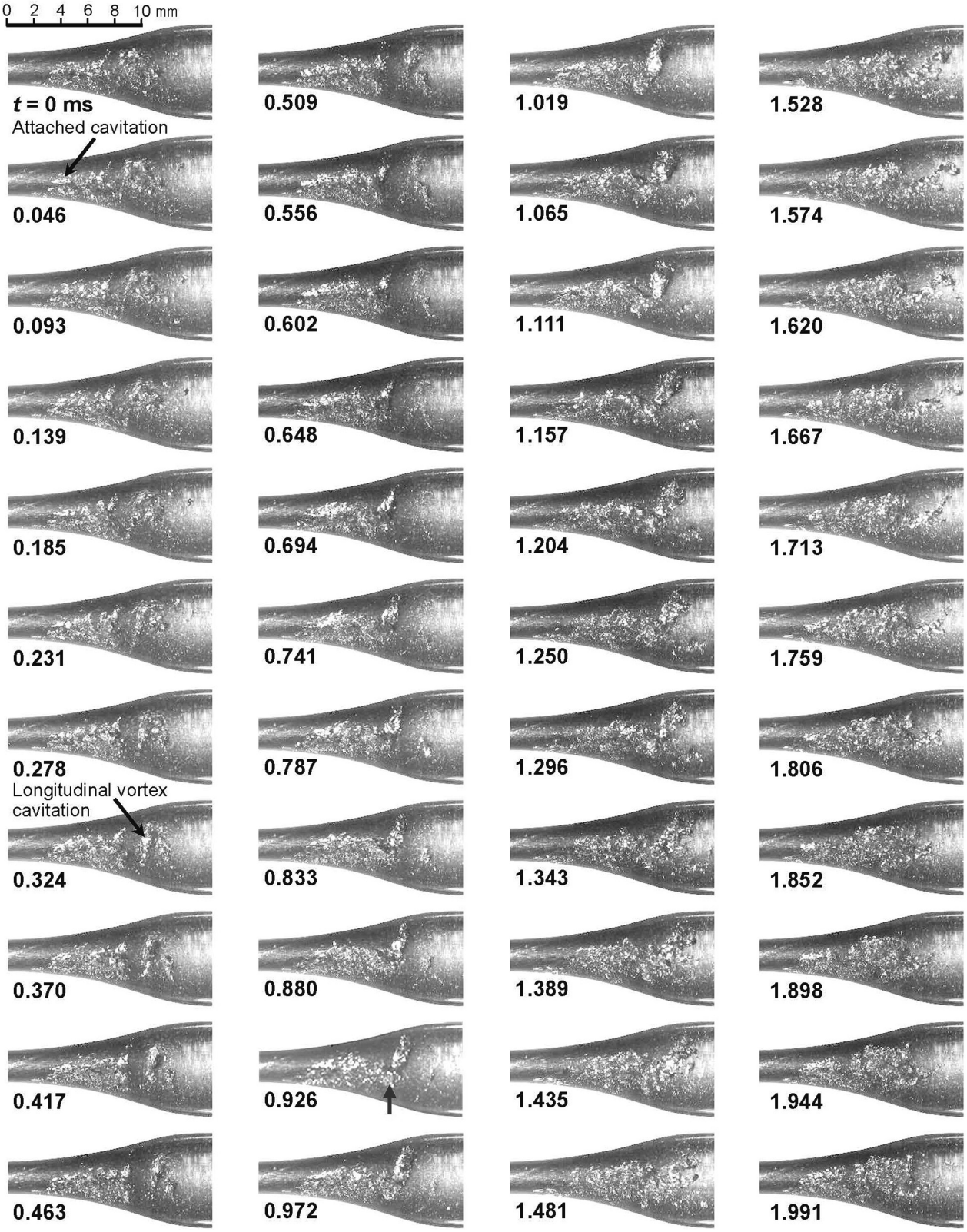

Fig. 9. Periodical shedding of typical vortex cavitation at $d = 2.0$ mm, $p_1 = 0.078$ MPa, $p_2 = 0.027$ MPa, $\sigma = 0.47$ observed by visible light.

considerably large, and cylindrical bubbles are aligned in the vortex core, then the shape of the bubbles of core looks like a spine. Some typical boundaries of the bubbles in vortex cavitation, such as those at 0.681, 0.868, and 0.926 ms in Fig. 10, appear as bamboo nodes. The vortex cavitation in Fig. 10 is also inclined 45° to the flow direction, as shown in Figs. 7 and 8. The diameter of the vaporized core of the vortex cavitation in Fig. 10 was about 1.2 mm at 0.681 ms and 0.8 mm at 0.926 ms. From these observations it is clear that the bubbles in the vortex core are not spherical bubbles, but consist rather of the angulated bubbles. This is very important for simulating the cavitating flow numerically, as

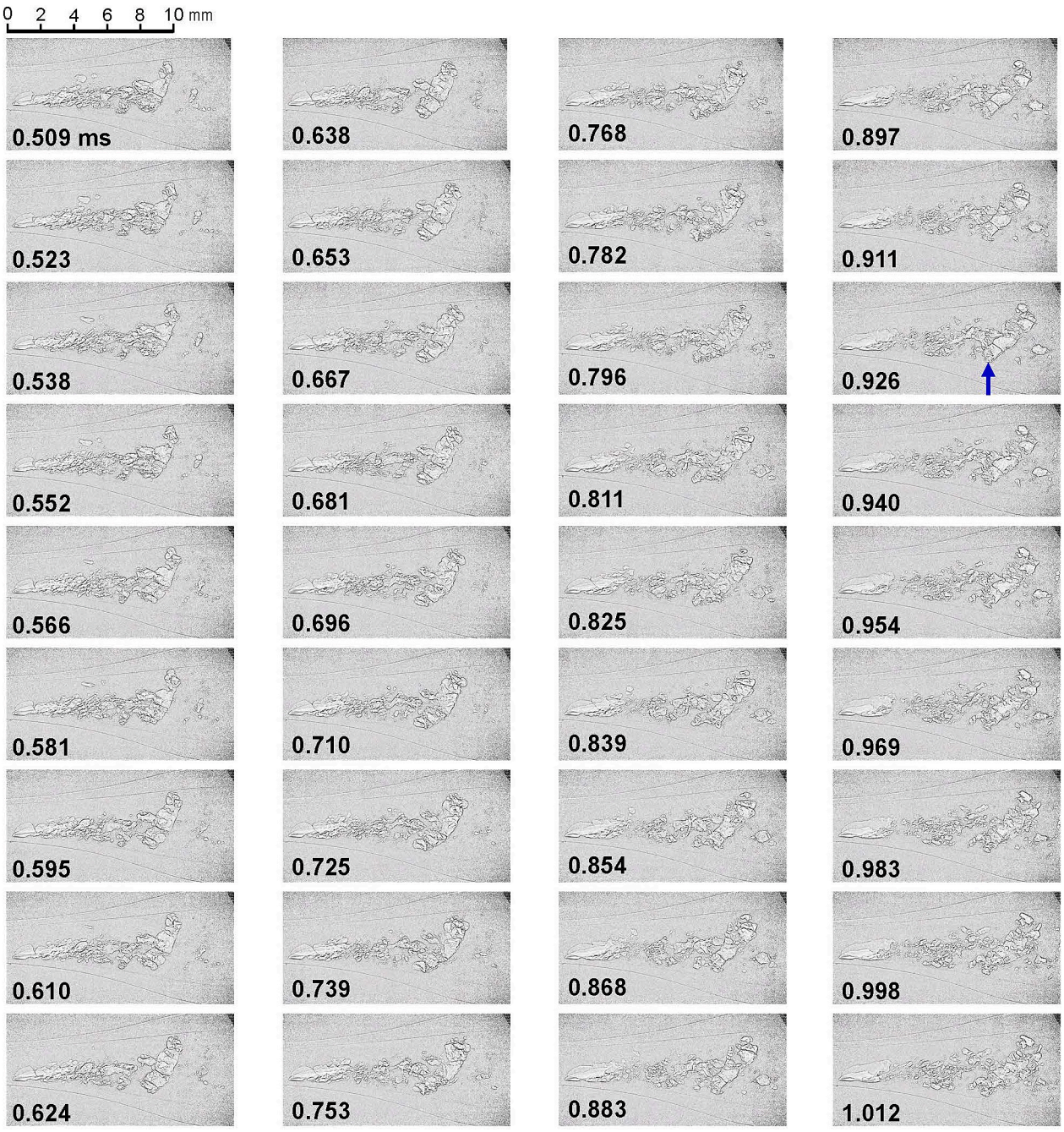

Fig. 10. One cycle of typical vortex cavitation from shedding of trailing edge to collapse at $d = 2.0$ mm, $p_1 = 0.078$ MPa, $p_2 = 0.027$ MPa, $\sigma = 0.47$ observed by high speed X-ray imaging.

the impact of bubble collapse near the solid wall strongly depends on the bubble shape [38,39].

3.4. Tangential velocity of vortex cavitation

To investigate the tangential velocity of the vortex cavitation, Fig. 11 shows the images taken at 1,128,668 fps, that is, an interval time of 886 ns, using X-rays at SPB/SFX, European-XFEL. The test condition was "No. 3" in Tables 1 and 2. The direction of the main flow through the Venturi tube was from left to right. As shown in Fig. 11, a typical vortex cavitation was observed, as shown in Figs. 7-10. The vortex cavitation shown in Fig. 11 also consisted of angulated bubbles, and the vortex core was inclined at 45° in the flow direction, as shown in Figs. 7-10. The maximum diameter of the vaporized core of the vortex cavitation was approximately 0.3 mm.

To obtain the tangential velocity of the surface of vortex cavitation, a distinctive area on the vortex cavitation surface was chosen, and the area was marked by green or yellow rectangles on the images from 20.378 μs to 28.352 μs. The observed moving velocity of the distinctive area was obtained by the positions of the distinctive area on images and the time interval of images. The dotted white line indicates the estimated vaporized vortex core. The shedding speed at the center of the vaporized vortex core in the flow direction was obtained by the position of vortex core and the time interval, and it was 17 ± 7 m/s. The observed moving velocity of the distinctive area on the vortex cavitation surface, obtained by moving the velocity of the area in the flow direction considering the vortex core inclination, was 29 ± 14 m/s. The observed moving velocity of the distinctive area included the shedding speed of

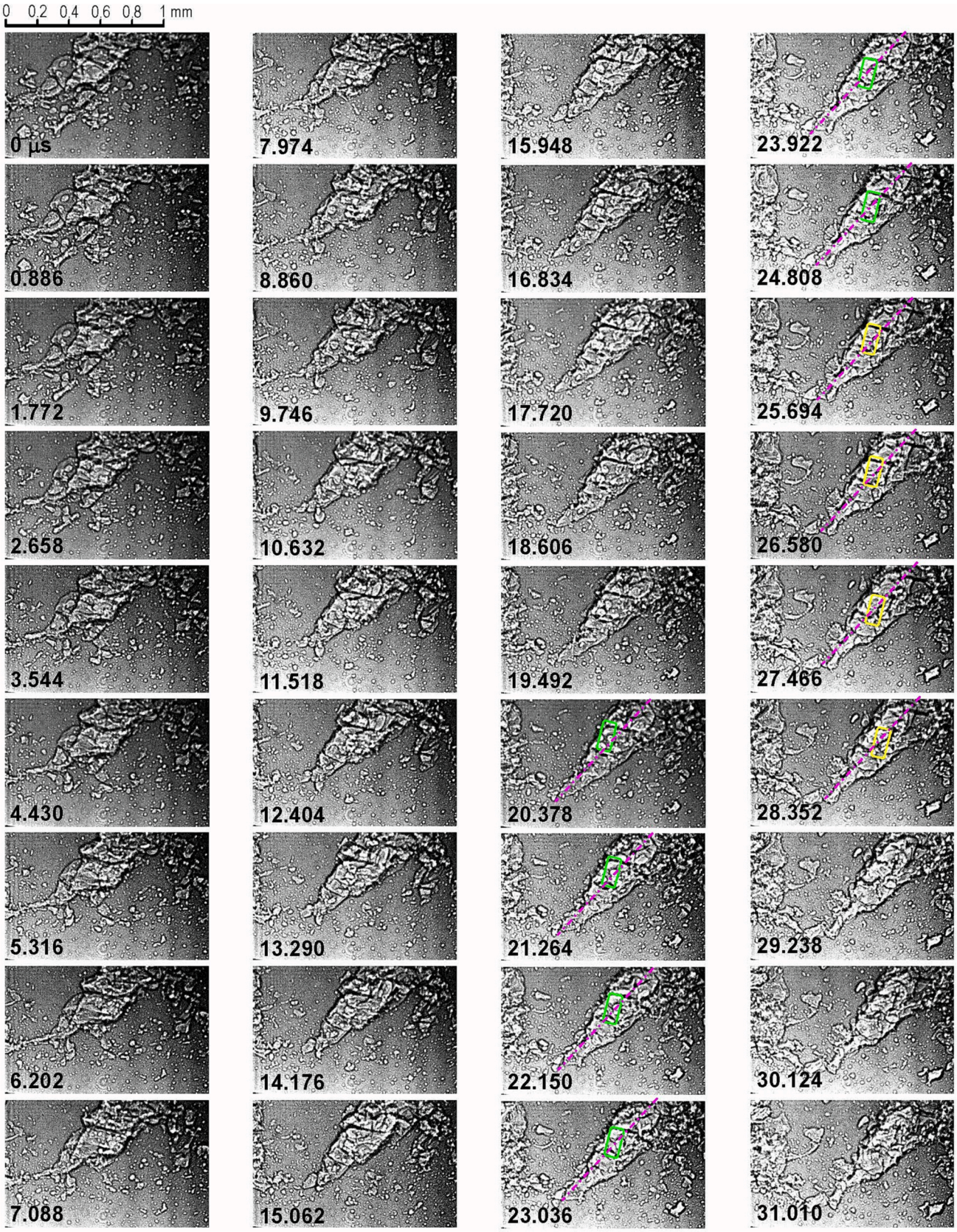

Fig. 11. Rotation of vortex cavitation arising in the Venturi tube observed by XFEL. (Test condition (3): $d = 0.5$, $p_1 = 0.35$ MPa, $p_2 = 0.1$ MPa)

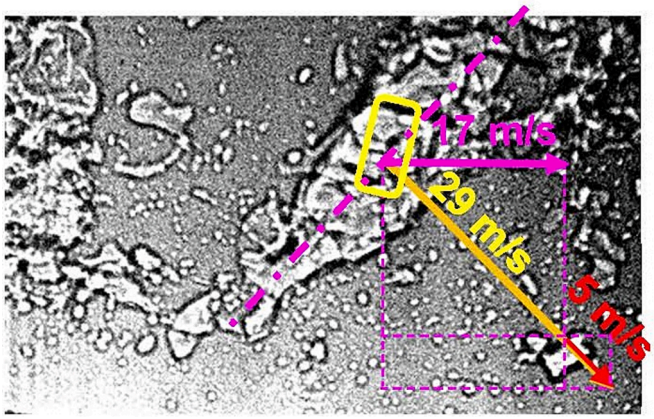

Fig. 12. Estimation of tangential velocity of vortex surface.

the vortex core, as shown in Fig. 12. The estimated tangential velocity of the surface of the vaporized vortex core was therefore approximately 5 m/s (≈ (29 – 17) / sin 45°).

4. Discussions

As mentioned in the introduction, vortex cavitation around the heart valve and/or tip vortex is assumed to be a Rankine vortex [72,73]. The tangential velocity of the surface of vortex cavitation in Figs. 11 and 12 are discussed considering the Rankine vortex. In the case of the Rankine vortex, the vortex is considered a combined vortex with an inner core and outer part, which is assumed to be an irrotational vortex (see Appendix A). Circumferential velocity v_θ was described as follows:

$$v_\theta = \omega r (r \le r_0) \tag{3}$$

$$v_\theta = \frac{C}{r} (r \ge r_0) \tag{4}$$

where r is the distance from the vortex center, r_0 is the combined position between the inner and outer layers, ω is the angular velocity at the inner core, and C is a constant. Pressure p can be expressed by the following equation:

$$p = p_0 + \frac{1}{2}\rho\omega^2 r^2 \quad (r \le r_0) \tag{5}$$

$$p = p_\infty - \frac{1}{2}\frac{\rho C^2}{r^2} \quad (r \ge r_0) \tag{6}$$

Here, p_0 is the pressure at vortex center, p_∞ is the pressure at $r \to \infty$, and p_∞ was assumed as $p_\infty = p_2$ in the present experiment. At $r = r_0$, v_θ and p are equivalent at the inner core and outer part, respectively; then,

$$C = \omega {r_0}^2 \tag{7}$$

$$p_\infty - p_0 = \rho\omega^2 {r_0}^2 \tag{8}$$

Thus, p at $r = r_0$ is obtained by substituting Eq. (7) into Eq. (6) as follows:

$$p = p_2 - \frac{1}{2}\rho\omega^2 {r_0}^2 \tag{9}$$

When it was assumed that it was cavitated at $r \le r_0$, i.e., $p = p_v$ at $r = r_0$, v_θ was denoted by the following equation.

$$v_\theta = \sqrt{\frac{2}{\rho}(p_2 - p_v)} \tag{10}$$

When $\rho = 9.98 \times 10^2$ kg/m^3, $p_2 = 0.1$ MPa, and $p_v = 2.49$ kPa were substituted into Eq. (10), $v_\theta = 14.0$ m/s was obtained. The observed velocity of the vortex surface was approximately 5 m/s, which was lower than 14 m/s. Thus, the observed vortex may include small air bubbles at initiation. When the distribution of local flow velocity around the vortex cavitation, which were shown in previous papers [16,79,80] was obtained by "correlation method," which was a digital image-processing technique for analyzing motion by means of a series of images [80], the tangential velocity was obtained for several vortex cavitation [80]. The measured velocity was lower than that of v_θ obtained by Rankin vortex model [81]. Namely, the previous results [81] also revealed the similar tendency of the present paper.

As shown in "*3.2. Attached cavitation and vortex cavitation*", there are two typical types of vortex cavitations: attached and vortex cavitation. One is the shedding from the trailing edge of the attached cavitation, and the other is initiated downstream of the attached cavitation. The former contains more air bubbles, that is, gaseous cavitation, whereas the latter contains fewer air bubbles, that is, vaporous cavitation. In the case of gaseous cavitation, the impact at the bubble collapse was weaker owing to the cushion effect [82]. Visualization of vortex cavitation by high-speed photography using X-rays has provided valuable information such as the bubble shape and tangential velocity of the vortex, which suggested the air content ratio in the vortex cavitation. It has been reported that one vortex cavitation out of 1000 generates an intense impact [29], and it is worthwhile to investigate vortex cavitation precisely using X-rays to improve the efficiency of chemical reactors and/or cavitation peening using hydrodynamic cavitation.

5. Conclusions

To investigate the structure of vortex cavitation, which is closely related to the cavitation intensity of chemical effects such as luminescence, the vortex cavitation of hydrodynamic cavitation arising in the Venturi tube was observed by high-speed photography using X-rays at SPring-8, Japan, and European-XFEL, Germany. The results are summarized as follows.

(1) The vortex cavitation arising in the Venturi tube consists of angulated bubbles rather than spherical bubbles.
(2) There are two typical types of vortices used for vortex cavitation generation. One was shed from the trailing edge of the attached cavitation developed near the throat. The other was generated in the downstream region of the attached cavitation owing to vortical flow and it might cause intense collapse due to lesser cushion effect.
(3) The vortex cavitation was shed periodically at stable injection pressure.
(4) The shedding frequency of the vortex cavitation depended on the geometry of the Venturi tube.
(5) The observed tangential velocity of the surface of vortex cavitation, whose vaporous diameter was 0.3 mm, was about 5 m/s.
(6) The vaporized core of a typical vortex cavitation was inclined 45° to the main flow direction.

CRediT authorship contribution statement

Hitoshi Soyama: Conceptualization, Formal analysis, Funding acquisition, Investigation, Methodology, Project administration, Resources, Visualization, Writing – original draft. **Xiaoyu Liang:** Data curation, Investigation, Methodology, Visualization, Writing – review & editing. **Wataru Yashiro:** Conceptualization, Funding acquisition, Investigation, Methodology, Supervision, Writing – review & editing. **Kentaro Kajiwara:** Investigation, Methodology. **Eleni Myrto Asimakopoulou:** Methodology. **Valerio Bellucci:** Investigation, Methodology. **Sarlota Birnsteinova:** Investigation, Methodology. **Gabriele Giovanetti:** Investigation, Methodology. **Chan Kim:** Investigation, Methodology. **Henry J. Kirkwood:** Data curation, Visualization. **Jayanath C.P. Koliyadu:** Investigation, Methodology. **Romain Letrun:**

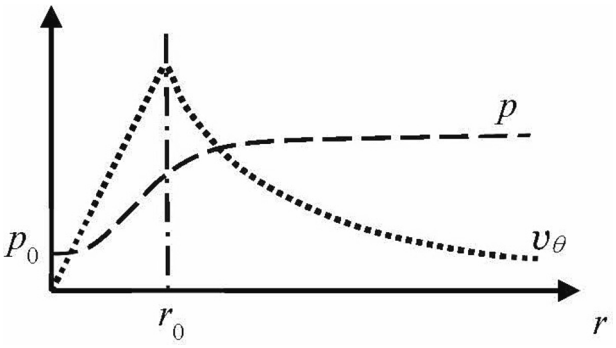

Fig. A1. Schematic of Rankine vortex.

Investigation, Methodology. **Yuhe Zhang:** Data curation. **Jozef Uličný:** Data curation, Project administration. **Richard Bean:** Methodology, Investigation. **Adrian P. Mancuso:** Methodology, Investigation. **Pablo Villanueva-Perez:** Methodology, Investigation, Funding acquisition. **Tokushi Sato:** Methodology, Investigation, Writing – review & editing. **Patrik Vagovič:** Conceptualization, Methodology, Investigation, Writing – review & editing, Project administration, Funding acquisition. **Daniel Eakins:** Conceptualization, Methodology, Writing – review & editing. **Alexander M. Korsunsky:** Conceptualization, Writing – review & editing, Supervision.

Declaration of competing interest

The authors declare that they have no known competing financial interests or personal relationships that could have appeared to influence the work reported in this paper.

Acknowledgments

The research was partly supported by Japan Science and Technology Agency (JST) CREST (JPMJCR1765) and JSPS KAKENHI (21H04530, 22KK0050 and 23H01292). Experiments were conducted at beamline 28B2 of SPring-8, Japan and SPB/SFX at European XFEL, Germany. We acknowledge European XFEL in Schenefeld, Germany, for the provision of X-ray free-electron laser beamtime at Scientific Instrument SPB/SFX and thank the staff for their assistance. This work received funding by HORIZON474 EIC-2021-PATHFINDEROPEN-01-01, MHz–TOMOSCOPY project, Grant agreement: 101046448; ERC-2020-STG, 3DXFLASH, Grant agreement 948426; EuXFEL R&D "MHz X-ray microscopy: From demonstration to method", 2020 - 2022; Bundesministerium für Bildung und Forschung (BMBF) (05K18XXA), Vetenskapsrådet (VR) (2017-06719), Röntgen Ångström Cluster INVISION project. PV acknowledge Thomas Dietze for technical support.

Appendix A. . Schematic of Rankine vortex

Fig. A1 illustrates the schematics of pressure p and circumferential velocity v_θ of a Rankine vortex changing with the distance from the vortex center r. As described in the main text, the Rankine vortex is a combined vortex with an inner core ($r \leq r_0$) and an outer part ($r \leq r_0$).

Appendix B. Supplementary data

Supplementary data to this article, that is videos of Figs. 5, 6, 7, 8, 9, 10, and 11, are found online in the electronic version. Supplementary data to this article can be found online at https://doi.org/10.1016/j.ultsonch.2023.106715.

References

[1] M. Gagol, A. Przyjazny, G. Boczkaj, Wastewater treatment by means of advanced oxidation processes based on cavitation - a review, Chem. Eng. J. 338 (2018) 599–627, https://doi.org/10.1016/j.cej.2018.01.049.
[2] H. Zheng, Y. Zheng, J. Zhu, Recent developments in hydrodynamic cavitation reactors: cavitation mechanism, reactor design, and applications, Engineering 19 (2022) 180–198, https://doi.org/10.1016/j.eng.2022.04.027.
[3] M.V. Bagal, P.R. Gogate, Wastewater treatment using hybrid treatment schemes based on cavitation and fenton chemistry: a review, Ultrason. Sonochem. 21 (2014) 1–14, https://doi.org/10.1016/j.ultsonch.2013.07.009.
[4] B. Wang, Y. Liu, H. Zhang, W. Shi, M. Xiong, C. Gao, M. Cui, Hydrodynamic cavitation and its application in water treatment combined with ozonation: a review, J. Ind. Eng. Chem. 114 (2022) 33–51, https://doi.org/10.1016/j.jiec.2022.07.031.
[5] Y. Chen, C. Yin, Y. Song, Application of hydrodynamic cavitation in the field of water treatment, Chem. Pap. 77 (2023) 3521–3546, https://doi.org/10.1007/s11696-023-02754-y.
[6] P.R. Gogate, A.M. Kabadi, A review of applications of cavitation in biochemical engineering/biotechnology, Biochem. Eng. J. 44 (2009) 60–72, https://doi.org/10.1016/j.bej.2008.10.006.
[7] M.A. Kelkar, P.R. Gogate, A.B. Pandit, Intensification of esterification of acids for synthesis of biodiesel using acoustic and hydrodynamic cavitation, Ultrason. Sonochem. 15 (2008) 188–194, https://doi.org/10.1016/j.ultsonch.2007.04.003.
[8] V. Innocenzi, M. Prisciandaro, Technical feasibility of biodiesel production from virgin oil and waste cooking oil: comparison between traditional and innovative process based on hydrodynamic cavitation, Waste Manag. 122 (2021) 15–25, https://doi.org/10.1016/j.wasman.2020.12.034.
[9] A. Ahmad, A.K. Yadav, A. Singh, A. Pal, Optimization of cavitation-assisted biodiesel production and fuel properties from neochloris oleoabundans microalgae oil using genetic algorithm and response surface methodology, Proc. Ins. Mech. Eng., Part e: J. Process Mech. Eng. (2023) 1–15, https://doi.org/10.1177/09544089231159832.
[10] A. Giuliano, C.M. Cellamare, L. Chiarini, S. Tabacchioni, L. Petta, Evaluation of the controlled hydrodynamic cavitation as gas mass transfer system for ex-situ biological hydrogen methanation, Chem. Eng. J. 471 (2023), 144475, https://doi.org/10.1016/j.cej.2023.144475.
[11] M. Deggelmann, J.A. Nopel, F. Rudiger, D. Paustian, P. Braeutigam, Hydrodynamic cavitation for micropollutant degradation in water - correlation of bisphenol a degradation with fluid mechanical properties, Ultrason. Sonochem. 83 (2022), 105950, https://doi.org/10.1016/j.ultsonch.2022.105950.
[12] C. Agarkoti, S.K. Gujar, P.R. Gogate, A.B. Pandit, Pilot scale degradation of sulfamerazine using different Venturi based hydrodynamic cavitation and ultrasound reactors in combination with oxidation processes, J. Environ. Chem. Eng. 11 (2023), 109857, https://doi.org/10.1016/j.jece.2023.109857.
[13] Z. Feng, F. Wang, K. Zhu, Z. Wang, J. Ning, Degradation of ammonia nitrogen by an economic combined hydrodynamic cavitation method, Environ. Sci. Pollut. Res. Int. 30 (2023) 72782–72792, https://doi.org/10.1007/s11356-023-27504-1.
[14] Y. Min Oo, K. Somnuk, Investigation of free fatty acid reduction from mixed crude palm oil using 3D-printed rotor-stator hydrodynamic cavitation: An experimental study of geometric characteristics of the inner hole, *Ultrason. Sonochem.* 98, (2023), 106472, 10.1016/j.ultsonch.2023.106472.
[15] S. Xu, J. Wang, W. Chen, B. Ji, H. Yan, Z. Zhang, X. Long, Removal of field-collected microcystis aeruginosa in pilot-scale by a jet pump cavitation reactor, Ultrason. Sonochem. 83 (2022), 105924, https://doi.org/10.1016/j.ultsonch.2022.105924.
[16] H. Soyama, Luminescence intensity of vortex cavitation in a Venturi tube changing with cavitation number, Ultrason. Sonochem. 71 (2021), 105389, https://doi.org/10.1016/j.ultsonch.2020.105389.
[17] J. Wang, H. Cheng, S. Xu, B. Ji, X. Long, Performance of cavitation flow and its induced noise of different jet pump cavitation reactors, Ultrason. Sonochem. 55 (2019) 322–331, https://doi.org/10.1016/j.ultsonch.2019.01.011.
[18] L. Liu, X. Yang, Y. Guo, B. Li, L.P. Wang, Reactive mixing performance for a nanoparticle precipitation in a swirling vortex flow reactor, Ultrason. Sonochem. 94 (2023), 106332, https://doi.org/10.1016/j.ultsonch.2023.106332.
[19] Y. Song, R. Hou, Z. Liu, J. Liu, W. Zhang, L. Zhang, Cavitation characteristics analysis of a novel rotor-radial groove hydrodynamic cavitation reactor, Ultrason. Sonochem. 86 (2022), 106028, https://doi.org/10.1016/j.ultsonch.2022.106028.
[20] M.H. Dehghani, R.R. Karri, J.R. Koduru, S. Manickam, I. Tyagi, N.M. Mubarak, Suhas, Recent trends in the applications of sonochemical reactors as an advanced oxidation process for the remediation of microbial hazards associated with water and wastewater: A critical review, Ultrason. Sonochem. 94 (2023), 106302, https://doi.org/10.1016/j.ultsonch.2023.106302.
[21] F. Duronio, A. Di Mascio, A. De Vita, V. Innocenzi, M. Prisciandaro, Eulerian-Lagrangian modeling of phase transition for application to cavitation-driven chemical processes, Phys. Fluids 35 (2023), 053305, https://doi.org/10.1063/5.0145568.
[22] A. Bampouli, Q. Goris, J. Van Olmen, S. Solmaz, M. Noorul Hussain, G.D. Stefanidis, T. Van Gerven, Understanding the ultrasound field of high viscosity mixtures: Experimental and numerical investigation of a lab scale batch reactor, *Ultrason. Sonochem.* 97, (2023), 106444, 10.1016/j.ultsonch.2023.106444.
[23] A.H. Thaker, V.V. Ranade, Emulsions using a vortex-based cavitation device: Influence of number of passes, pressure drop, and device scale on droplet size distributions, *Ind. Eng. Chem. Res.* (2022), A-O, 10.1021/acs.iecr.2c03714.
[24] P. Pipp, M. Hocevar, M. Dular, Challenges of numerical simulations of cavitation reactors for water treatment - an example of flow simulation inside a cavitating

microchannel, Ultrason. Sonochem. 77 (2021), 105663, https://doi.org/10.1016/j.ultsonch.2021.105663.
[25] M. Ge, C. Sun, G. Zhang, O. Coutier-Delgosha, D. Fan, Combined suppression effects on hydrodynamic cavitation performance in Venturi-type reactor for process intensification, Ultrason. Sonochem. 86 (2022), 106035, https://doi.org/10.1016/j.ultsonch.2022.106035.
[26] F. Hong, H. Xue, X. Yuan, L. Wang, H. Tian, L. Ye, J. Jia, D. Ying, Y. Huang, Numerical investigation on the hydrodynamic performance with special emphasis on the cavitation intensity detection in a Venturi cavitator, Process Saf. Environ. Prot. 175 (2023) 212–226, https://doi.org/10.1016/j.psep.2023.05.037.
[27] F. Hong, H. Tian, X. Yuan, S. Liu, Q. Peng, Y. Shi, L. Jin, L. Ye, J. Jia, D. Ying, T. S. Ramsey, Y. Huang, CFD-assisted modeling of the hydrodynamic cavitation reactors for wastewater treatment - a review, J. Environ. Manage. 321 (2022), 115982, https://doi.org/10.1016/j.jenvman.2022.115982.
[28] S. Lesnik, A. Aghelmaleki, R. Mettin, G. Brenner, Modeling acoustic cavitation with inhomogeneous polydisperse bubble population on a large scale, Ultrason. Sonochem. 89 (2022), 106060, https://doi.org/10.1016/j.ultsonch.2022.106060.
[29] H. Soyama, A.M. Korsunsky, A critical comparative review of cavitation peening and other surface peening methods, J. Mater. Process. Technol. 305 (2022), 117586, https://doi.org/10.1016/j.jmatprotec.2022.117586.
[30] T. Okada, Y. Iwai, S. Hattori, N. Tanimura, Relation between impact load and the damage produced by cavitation bubble collapse, Wear 184 (1995) 231–239, https://doi.org/10.1016/0043-1648(94)06581-0.
[31] A. Kubota, H. Kato, H. Yamaguchi, A new modeling of cavitating flows - a numerical study of unsteady cavitation on a hydrofoil section, J. Fluid Mech. 240 (1992) 59–96, https://doi.org/10.1017/s002211209200003x.
[32] B. Ji, X. Luo, R.E.A. Arndt, Y. Wu, Numerical simulation of three dimensional cavitation shedding dynamics with special emphasis on cavitation–vortex interaction, Ocean Eng. 87 (2014) 64–77, https://doi.org/10.1016/j.oceaneng.2014.05.005.
[33] J.S. Ma, C.T. Hsiao, G.L. Chahine, Numerical study of acoustically driven bubble cloud dynamics near a rigid wall, Ultrason. Sonochem. 40 (2018) 944–954, https://doi.org/10.1016/j.ultsonch.2017.08.033.
[34] H.Y. Cheng, X.R. Bai, X.P. Long, B. Ji, X.X. Peng, M. Farhat, Large eddy simulation of the tip-leakage cavitating flow with an insight on how cavitation influences vorticity and turbulence, App. Math. Model. 77 (2020) 788–809, https://doi.org/10.1016/j.apm.2019.08.005.
[35] Y. Shi, K. Luo, X. Chen, D. Li, L. Jia, A new cavitation model considering inter-bubble action, *International Journal of Naval Architecture and Ocean*, Engineering 13 (2021) 566–574, https://doi.org/10.1016/j.ijnaoe.2021.05.005.
[36] T. Yamamoto, S.V. Komarov, Enhancement of oscillation amplitude of cavitation bubble due to acoustic wake effect in multibubble environment, Ultrason. Sonochem. 78 (2021), 105734, https://doi.org/10.1016/j.ultsonch.2021.105734.
[37] K. Okita, Y. Miyamoto, T. Furukawa, S. Takagi, Numerical study on stress in a solid wall caused by the collapse of a cavitation bubble cloud in hydraulic fluid, Int. J. Multiph. Flow 150 (2022), 103965, https://doi.org/10.1016/j.ijmultiphaseflow.2021.103965.
[38] S.R. Gonzalez-Avila, F. Denner, C.-D. Ohl, The acoustic pressure generated by the cavitation bubble expansion and collapse near a rigid wall, Phys. Fluids 33 (2021), https://doi.org/10.1063/5.0043822.
[39] Y. Iga, H. Sasaki, Relationship between a non-spherical collapse of a bubble and a stress state inside a wall, Phys. Fluids 35 (2023), 023312, https://doi.org/10.1063/5.0136355.
[40] H. Cheng, X. Long, B. Ji, X. Peng, M. Farhat, A new euler-lagrangian cavitation model for tip-vortex cavitation with the effect of non-condensable gas, Int. J. Multiph. Flow 134 (2021), https://doi.org/10.1016/j.ijmultiphaseflow.2020.103441.
[41] R.E.A. Arndt, Cavitation in vortical flows, Annu. Rev. Fluid Mech. 34 (2002) 143–175, https://doi.org/10.1146/annurev.fluid.34.082301.114957.
[42] R.E.A. Arndt, V.H. Arakeri, H. Higuchi, Some observations of tip-vortex cavitation, J. Fluid Mech. 229 (1991) 269–289, https://doi.org/10.1017/s0022112091003026.
[43] Y. Kawanami, H. Kato, H. Yamaguchi, M. Maeda, S. Nakasumi, Inner structure of cloud cavity on a foil section, *JSME Inter*, J. Ser. B-Fluids and Thermal Engineering 45 (2002) 655–661, https://doi.org/10.1299/jsmeb.45.655.
[44] B. Huang, S.-C. Qiu, X.-B. Li, Q. Wu, G.-Y. Wang, A review of transient flow structure and unsteady mechanism of cavitating flow, J. Hydrodyn. 31 (2019) 429–444, https://doi.org/10.1007/s42241-019-0050-0.
[45] B. Tian, L. Li, Y. Meng, B. Huang, Multiscale modeling of different cavitating flow patterns around NACA66 hydrofoil, Phys. Fluids 34 (2022), 103322, https://doi.org/10.1063/5.0117162.
[46] Z. Wang, H. Cheng, B. Ji, X. Peng, Numerical investigation of inner structure and its formation mechanism of cloud cavitating flow, Int. J. Multiph. Flow 165 (2023), 103322, https://doi.org/10.1016/j.ijmultiphaseflow.2023.104484.
[47] J. Chen, B. Huang, T. Liu, Y. Wang, G. Wang, Numerical investigation of cavitation-vortex interaction with special emphasis on the multistage shedding process, App. Math. Model. 96 (2021) 111–130, https://doi.org/10.1016/j.apm.2021.02.003.
[48] B. Stutz, S. Legoupil, X-ray measurements within unsteady cavitation, Exp. Fluids 35 (2003) 130–138, https://doi.org/10.1007/s00348-003-0622-0.
[49] O. Coutier-Delgosha, J.L. Reboud, Y. Delannoy, Numerical simulation of the unsteady behaviour of cavitating flows, Int. J. Numer. Meth. Fluids 42 (2003) 527–548, https://doi.org/10.1002/fld.530.
[50] O. Coutier-Delgosha, B. Stutz, A. Vabre, S. Legoupil, Analysis of cavitating flow structure by experimental and numerical investigations, J. Fluid Mech. 578 (2007) 171–222, https://doi.org/10.1017/s0022112007004934.
[51] H. Ganesh, S.A. Mäkiharju, S.L. Ceccio, Bubbly shock propagation as a mechanism for sheet-to-cloud transition of partial cavities, J. Fluid Mech. 802 (2016) 37–78, https://doi.org/10.1017/jfm.2016.425.
[52] S.A. Mäkiharju, H. Ganesh, S.L. Ceccio, The dynamics of partial cavity formation, shedding and the influence of dissolved and injected non-condensable gas, J. Fluid Mech. 829 (2017) 420–458, https://doi.org/10.1017/jfm.2017.569.
[53] S. Yoon, S.A. Makiharju, J.A. Fessler, S.L. Ceccio, Image reconstruction for limited-angle electron beam X-ray computed tomography with energy-integrating detectors for multiphase flows, IEEE Trans. Comput. Imaging 4 (2018) 112–124, https://doi.org/10.1109/tci.2017.2775603.
[54] J. Wu, H. Ganesh, S. Ceccio, Multimodal partial cavity shedding on a two-dimensional hydrofoil and its relation to the presence of bubbly shocks, Exp. Fluids 60 (2019), https://doi.org/10.1007/s00348-019-2706-5.
[55] A. Bhatt, H. Ganesh, S.L. Ceccio, Cavitating flow behind a backward facing step, *Int. J. Multiph. Flow* 139, (2021), 60:60, 10.1016/j.ijmultiphaseflow.2021.103584.
[56] A. Bhatt, H. Ganesh, S.L. Ceccio, Partial cavity shedding on a hydrofoil resulting from re-entrant flow and bubbly shock waves, J. Fluid Mech. 957 (2023) A28, https://doi.org/10.1017/jfm.2022.999.
[57] A. Vabre, M. Gmar, D. Lazaro, S. Legoupil, O. Coutier, A. Dazin, W.K. Lee, K. Fezzaa, Synchrotron ultra-fast X-ray imaging of a cavitating flow in a venturi profile, Nucl. Instrum. Methods Phys. Res., Sect. A 607 (2009) 215–217, https://doi.org/10.1016/j.nima.2009.03.192.
[58] Z. Izadifar, G. Belev, M. Izadifar, Z. Izadifar, D. Chapman, Visualization of ultrasound induced cavitation bubbles using the synchrotron X-ray analyzer based imaging technique, Phys Med Biol 59 (2014) 7541–7555, https://doi.org/10.1088/0031-9155/59/23/7541.
[59] W.W. Xu, I. Tzanakis, P. Srirangam, W.U. Mirihanage, D.G. Eskin, A.J. Bodey, P. D. Lee, Synchrotron quantification of ultrasound cavitation and bubble dynamics in Al-10Cu melts, Ultrason Sonochem 31 (2016) 355–361, https://doi.org/10.1016/j.ultsonch.2016.01.017.
[60] L. Qin, B.M. Maciejewska, T. Subroto, J.A. Morton, K. Porfyrakis, I. Tzanakis, D. G. Eskin, N. Grobert, K. Fezzaa, J. Mi, Ultrafast synchrotron X-ray imaging and multiphysics modelling of liquid phase fatigue exfoliation of graphite under ultrasound, Carbon 186 (2022) 227–237, https://doi.org/10.1016/j.carbon.2021.10.014.
[61] L. Qin, K. Porfyrakis, I. Tzanakis, N. Grobert, D.G. Eskin, K. Fezzaa, J. Mi, Multiscale interactions of liquid, bubbles and solid phases in ultrasonic fields revealed by multiphysics modelling and ultrafast X-ray imaging, Ultrason Sonochem 89 (2022), 106158, https://doi.org/10.1016/j.ultsonch.2022.106158.
[62] I. Khlifa, A. Vabre, M. Hočevar, K. Fezzaa, S. Fuzier, O. Roussette, O. Coutier-Delgosha, Fast X-ray imaging of cavitating flows, Exp. Fluids 58 (2017) 157, https://doi.org/10.1007/s00348-017-2426-7.
[63] G. Zhang, I. Khlifa, O. Coutier-Delgosha, A comparative study of quasi-stable sheet cavities at different stages based on fast synchrotron X-ray imaging, Phys. Fluids 32 (2020), 123316, https://doi.org/10.1063/5.0031433.
[64] G. Zhang, I. Khlifa, K. Fezzaa, M. Ge, O. Coutier-Delgosha, Experimental investigation of internal two-phase flow structures and dynamics of quasi-stable sheet cavitation by fast synchrotron X-ray imaging, Phys. Fluids 32 (2020), 113310, https://doi.org/10.1063/5.0029963.
[65] I.K. Karathanassis, M. Heidari-Koochi, Q. Zhang, J. Hwang, P. Koukouvinis, J. Wang, M. Gavaises, X-ray phase contrast and absorption imaging for the quantification of transient cavitation in high-speed nozzle flows, Phys. Fluids 33 (2021), 032102, https://doi.org/10.1063/5.0038475.
[66] D. Podbevšek, M. Petkovšek, C.D. Ohl, M. Dular, Kelvin-Helmholtz instability governs the cavitation cloud shedding in venturi microchannel, Int. J. Multiph. Flow 142 (2021), 103700, https://doi.org/10.1016/j.ijmultiphaseflow.2021.103700.
[67] W. Voegeli, K. Kajiwara, H. Kudo, T. Shirasawa, X. Liang, W. Yashiro, Multibeam X-ray optical system for high-speed tomography, Optica 7 (2020), 384804, https://doi.org/10.1364/optica.384804.
[68] X. Liang, W. Voegeli, H. Kudo, E. Arakawa, T. Shirasawa, K. Kajiwara, T. Abukawa, W. Yashiro, Sub-millisecond 4D X-ray tomography achieved with a multibeam X-ray imaging system, *Applied Physics Express* 16, (2023), 072001, 10.35848/1882-0786/ace0f2.
[69] P. Villanueva-Perez, Y.Z. Valerio Bellucci, S. Birnsteinova, L.A. Rita Graceffa, E.M. Asimakopoulou, I. Petrov, Z. Yao, M. Romagnoni, A. Mazzolari, R. Letrun, C. Kim, J.C.P. Koliyadu, C. Deiter, R. Bean, G. Giovanetti, L. Gelisio, T. Ritschel, A. Mancuso, H.N. Chapman, A. Meents, T. Sato, P. Vagovic, Megahertz X-ray multi-projection imaging, *arXiv:2305.11920v1* (2023), 10.48550/arXiv.2305.11920.
[70] H. Soyama, J. Hoshino, Enhancing the aggressive intensity of hydrodynamic cavitation through a Venturi tube by increasing the pressure in the region where the bubbles collapse, AIP Adv. 6 (2016), 045113, https://doi.org/10.1063/1.4947572.
[71] C. Kang, H.X. Liu, H. Soyama, Estimation of aggressive intensity of a cavitating jet with multiple experimental methods, Wear 394 (2018) 176–186, https://doi.org/10.1016/j.wear.2017.11.001.
[72] C.P. Li, S.F. Chen, C.W. Lo, P.C. Lu, Role of vortices in cavitation formation in the flow at the closure of a bileaflet mitral mechanical heart valve, J. Artif. Organs 15 (2012) 57–64, https://doi.org/10.1007/s10047-011-0612-6.
[73] J. Park, W. Seong, Novel scaling law for estimating propeller tip vortex cavitation noise from model experiment, J. Hydrodyn. 29 (2017) 962–971, https://doi.org/10.1016/s1001-6058(16)60810-7.
[74] A.P. Mancuso, A. Aquila, L. Batchelor, R.J. Bean, J. Bielecki, G. Borchers, K. Doerner, K. Giewekemeyer, R. Graceffa, O.D. Kelsey, Y. Kim, H.J. Kirkwood, A. Legrand, R. Letrun, B. Manning, L. Lopez Morillo, M. Messerschmidt, G. Mills, S. Raabe, N. Reimers, A. Round, T. Sato, J. Schulz, C. Signe Takem, M. Sikorski, S.

Stern, P. Thute, P. Vagovic, B. Weinhausen, T. Tschentscher, The single particles, clusters and biomolecules and serial femtosecond crystallography instrument of the european XFEL: Initial installation, *J. Synchrotron Radiat.* 26, (2019), 660-676, 10.1107/S1600577519003308.

[75] J.R. Taylor, An introduction to error analysis, the study of uncertainties in physical measurements, University Science Books, 1982.

[76] P. Vagovič, T. Sato, L. Mikeš, G. Mills, R. Graceffa, F. Mattsson, P. Villanueva-Perez, A. Ershov, T. Faragó, J. Uličný, H. Kirkwood, R. Letrun, R. Mokso, M.-C. Zdora, M.P. Olbinado, A. Rack, T. Baumbach, J. Schulz, A. Meents, H. N. Chapman, A.P. Mancuso, Megahertz X-ray microscopy at X-ray free-electron laser and synchrotron sources, Optica 6 (2019) 1106, https://doi.org/10.1364/optica.6.001106.

[77] Y. Ito, R. Oba, H. Soyama, H. Ogata, T. Okamura, S. Sudo, R. Ikeda, A study on cavitation scale effects especially with respect to cavitation-induced high-pressure pulses, Trans. JSME 54B (1988) 2727–2733, https://doi.org/10.1299/kikaib.54.2727.

[78] M. Dular, M. Petkovšek, On the mechanisms of cavitation erosion – coupling high speed videos to damage patterns, Exp. Therm. Fluid Sci. 68 (2015) 359–370, https://doi.org/10.1016/j.expthermflusci.2015.06.001.

[79] H. Soyama, K. Ohba, S. Takeda, R. Oba, High-speed observations of highly erosive vortex cavitation around butterfly valve, Trans. JSME 60B (1994) 1133–1138. https://www.jstage.jst.go.jp/article/kikaib1979/60/572/60_572_1133/_pdf/-char/ja.

[80] K. Ohba, H. Soyama, S. Takeda, H. Inooka, R. Oba, High-speed observations of highly erosive vortex cavitation using image processing, Journal of Flow Visualization and Image Processing 2 (1995) 161–172, https://doi.org/10.1615/JFlowVisImageProc.v2.i2.50.

[81] H. Soyama, K. Ohba, T. Ikohagi, R. Oba, Behavior of severe erosive vortex cavitation : Local velocity distribution around vortex, Turbomachinery 23 (1995) 315–318. https://www.jstage.jst.go.jp/article/tsj1973/23/6/23_6_315/_pdf.

[82] H. Soyama, Y. Iga, Laser cavitation peening: A review, Appl. Sci. 13 (2023) 6702, https://doi.org/10.3390/app13116702.